BNL-NUREG-25716

CONF-
790808--6

MASTER

EXPERIMENTAL INVESTIGATIONS OF NONEQUILIBRIUM FLASHING OF WATER IN A CONVERGING-DIVERGING NOZZLE*

By

G. A. Zimmer, B.J.C. Wu, W. J. Leonhardt
N. Abuaf and O. C. Jones, Jr.

Thermal Hydraulic Development Division
Department of Nuclear Energy
Brookhaven National Laboratory
Upton, New York 11973

FEBRUARY 1979

*Work Performed Under the Auspices of the U.S. Nuclear Regulatory Commission.

ABSTRACT

A steady water loop with well controlled flow and thermodynamic conditions was designed, built, and made operational to measure the net vapor generation rates under nonequilibrium conditions. The test section consists of a converging-diverging nozzle with 49 pressure taps and observation windows at the exit. First pressure distributions and photographic observations were recorded under various flashing conditions. The effect of the various parameters such as inlet pressure, inlet temperature, mass flux, and back pressure on the pressure distributions and flashing regimes have been investigated and are reported here. Under specific flashing conditions, a sharp increase in pressure (condensation shock) was observed in the diverging section (which accommodates the high back pressures).

The experiments are being continued with a γ densitometer to measure the void fraction distributions needed in the vapor generation rate calculations.

INTRODUCTION

Several experimental, as well as analytical investigations have been undertaken to date in order to accurately calculate the discharge flow rates of two-phase mixtures from pipes, nozzles, and orifices. This problem presents itself in the safety analysis of water cooled nuclear reactors and also in the safe storage and handling of liquid cryogens in space applications.

During a nuclear reactor hypothetical loss-of-coolant accident (LOCA), the flow is expected to be choked at the break. The discharge flow rate affects the heat transfer in the core, the depressurization rate of the containment vessel, and it dictates the design requirements of the emergency core cooling system. Theoretical models have been proposed, and large computer codes have been developed, to predict the critical flow rates and their dependence on the upstream thermodynamic and flow conditions, as well as the pipe size and system geometry. At present, there is no general model or correlation for critical flows which considers both thermal nonequilibrium and relative velocities between the phases and which is valid for a wide range of pipe lengths, diameters, and upstream conditions, including subcooled liquid. A modeling effort combined with well-controlled experiments is currently being undertaken at Brookhaven National Laboratory, to investigate and measure the actual vapor generation rates under nonequilibrium conditions. The purpose of this paper is to describe the test facility, including the venturi test section and loop instrumentation, as well as to present the experimental results and photographic observations accomplished to date under nonequilibrium flashing conditions.

REVIEW OF THE LITERATURE

Extensive analytical and experimental work has been reported on the two-phase critical flows in the last three decades. Thorough reviews have been presented by Hsu (1972) and Saha (1978). The latter author summarized the various available critical flow models and emphasized the effects of thermal nonequilibrium and relative velocities between the phases, which become prominent under certain conditions. Since the objective of the present research was the determination of the vapor generation rates under nonequilibrium conditions, we will concentrate on pertinent experimental work in the literature.

To study flashing flows and critical flow conditions, researchers have used several kinds of test facilities. Some use an upstream vessel containing a saturated or subcooled liquid, which expands in the test section. Others have used systems where the two phases are generated separately and then mixed together before being introduced into the test section. When either system is operated as a once-through experiment, the flow from the test section discharges into a downstream container whose pressure can be adjusted independently of the upstream conditions. When either system is operated in steady, closed loops, the control of the downstream pressure independently of the upstream conditions becomes more difficult to achieve due to the hydraulic coupling of the test section with the loop.

In this paper, we will consider only experiments conducted with subcooled or saturated inlet conditions. The various test sections investigated to date can be classified as: first, long tubes and nozzles; second, short tubes and short nozzles; and third, orifices.

Long tubes and nozzles can be characterized by $L/D > 40$ (Seynhaeve 1977). Such experiments were conducted by Isbin, Moy and DaCruz (1957), James (1962), Fauske (1965), Reocreux and Seynhaeve (1974), Ardron and Ackerman (1978), etc. Reocreux (1974) was the first researcher to provide pressure measurements, as well as void fraction distributions which allow the direct calculation of the vapor generation rates, provided a specific slip model is adopted. In all of the experiments conducted with long straight pipes, the friction effects are equally important as the vapor generation rate to the choking condition, and thus the vapor generation effect can not be singled out easily.

Short tubes and nozzles with $1 < L/D < 40$ have also been extensively investigated by Silver (1948), Zaloudek (1963), Fauske and Henry (1971), and Schrock, Starkman and Brown (1977). Similar choked flow experiments were also reported by Simoneau (1975) and Hendrick, Simoneau, and Barrows (1976) with cryogenic liquids. Although these experiments with a converging diverging nozzle can provide a lot of information on the flashing inception, vapor generation rates and choking conditions, no detailed void fraction measurements were performed by the researchers except by Reocreux (1974) who performed his experiments in a long tube.

Orifices with $L/D < 1$ were usually placed in a uniform cross section tube, and the jet has been investigated by several authors. More recently, Seynhaeve (1977) measured axial and radial void fractions of the jet, in addition to the pressure distributions.

EXPERIMENTAL TECHNIQUES

A. Flow Loop

The main flow loop presented in Fig. 1 is constructed from "three inch" nominal (7.6 cm) stainless steel pipe. High purity water is circulated through the loop using a centrifugal pump rated at 1500 ℓ/min at a head of 600 kPa.

Starting from the pump, the fluid passes through a flow control station where the flow rate can be controlled from 3 to 950 ℓ/min and measured with an accuracy of 1/2 percent of actual flow rate. Excess flow from the pump is directed to secondary loops for cooling, purification and simple bypass flow routing. After the flow rate is set and measured, the fluid passes through the heater system where up to 520 kW of heat can be added to the flow, and the outlet temperature can be regulated to $\pm$ 0.3°K over the entire controlled flow range.

Leaving the heater system, the fluid passes through the test section. A pressurizer is connected to the main loop between the heater system and the test section and, when valved in, the pressurizer fixes the inlet pressure to the test section. Alternately, the pressurizer may be isolated from the loop by turning the valve off. In this fashion, the flow in the loop is controlled by the pump flow rate. Thus, two modes of operation are possible: the pressure controlled and the flow controlled modes. Once the fluid has passed through the test section, it enters a condensing tank where a cooling spray is utilized to condense the vapor and to fix the tank temperature. Since the pressure in the tank is essentially the same as in

the test section exit, the condensing tank and pressurizer can be used together to fix the pressure drop across the test section.

The fluid travels, after leaving the condensing tank, back to the pump, and, depending on conditions, cooling water can be added to this flow to prevent cavitation in the pump. Cooling water is provided from pump excess flow and is cooled by shell and tube heat exchangers tied to a 730 kW cooling tower.

Purification of the test fluid is accomplished during initial filling of the test loop. The water is deoxidized, deionized and passed through 0.22 micron filters. In addition, about 40 ℓ/min of excess pump flow is passed through the purification station as a polishing procedure during flow loop operation.

B. Test Section

The test section is a stainless steel tube, 78.7 cm long, and has a portion which forms a venturi. This converging/diverging portion is 55.9 cm long and has inside diameters of 5.1 cm at the ends and 2.5 cm at the throat. The wall thickness varies only from 0.57 mm to 0.60 mm over the entire tube length.

The test section design and construction were performed in three levels each with increased complexity in instrumentation. In the first level, 49 pressure taps (0.4 mm in diameter) were installed on 1.3 cm centers along the length of the venturi, in addition to a set of observation windows located 15 cm downstream of the test section exit, which allowed photographic observations by flash photography. In the second level, a single

channel (i.e., single beam) gamma densitometer was added which can be traversed virtually everywhere within the test section. As the system develops, the single beam densitometer will be replaced by two banks of five beams each for more efficient data taking and cross correlation. A hydrofoil-like probe containing ten pairs of local sensors is the third level of construction, and it will allow the measurement of local void fractions and phase velocities across a particular diameter and along the entire axis of the test section.

Presently pressure distribution data has been taken, and the flashing regimes were recorded photographically by means of a flash and a still camera arrangement located downstream of the test section outlet.

C. Loop Operation Conditions and Instrumentation

The loop operation conditions are summarized in Table I. The inlet pressure and temperature can be varied from 100-1000 kPa and from room temperature to 150°C respectively. The inlet mass flux covers a range of 1.1-7.9 Mg/m^2s. These operation limits cover a Reynolds number range of 10^5-10^6 based on test section inlet conditions. The various loop instrumentation, including ranges and accuracies, are tabulated in Table II. Pressure measurements are accomplished by means of Statham gauges, each calibrated to an accuracy better than 0.1 percent of the reading. The temperatures are measured by thermocouples and RTD's, and the flow rate measurements are performed by two Cox turbine flow meters, upstream of the test section.

DATA ACQUISITION

A. General Data Acquisition System

The centralized Data Acquisition and Data Analysis System (DADAS) was designed as a real time digital data system with multiterminal multitasking capability. The system was constructed around a Hewlett Packard 9640 system 1000 consisting of a 21MX minicomputer with 112 kilowords of central memory, 7.5 megaword cartridge discs, 9 track magnetic tape transport and paper tape I/O. Central control of the system is accomplished with a CRT terminal while the 3 satellite stations employ silent 700 terminals. Tabular and graphical presentation of data is achieved with a Varian electrostatic printer/plotter capable of listing 600 LPM and plotting 1.6 ips. Interface of the ADC systems is both direct, an interface per device, and via the universal interface bus, IEEE standard 488.

Three levels of ADC speed and resolution are incorporated within DADAS. The slow speed, high resolution system employs an integrating digital voltmeter with microvolt resolution and 300 channel guarded crossbar scanner. The through-put rate of this system is up to 18 measurements per second with high common mode voltage rejection capability. The intermediate speed system is a 15 bit ($\pm$ 10.24 volts) multiplexed ADC with a 50 kHz through-put rate. The system employs a single programmable gain amplifier and a signal conditioning amplifier and filter per channel. The system has high common mode voltage rejection capability and can be connected directly to experiments. The high speed system is also a 15 bit ($\pm$ 10.24 volt) multiplexed ADC with a 500 kHz through-put rate. The system has eight input

channels with simultaneous sample and hold amplifiers. This system was designed specifically for digitizing analog tapes.

B. Static Pressure Measurement Set-Up

Each of the 49 pressure taps on the test section can be connected through two manifolds and two hand operated valves to the low or high pressure sides of a pressure transducer bank. The differential pressure across two locations along the test section can be measured by connecting the two taps to the low and high sides of the pressure transducer. Six Statham pressure transducers with the ranges of 17, 34, 69, 172, 344, and 687 kPa (2.5, 5, 10, 25, 50, 100 psi) were connected in parallel to the two pressure measuring manifolds through two solenoid valves. A third solenoid valve in each transducer allows the shorting of the high and low pressure lines and thus provides a means of measuring and monitoring the zero point stability of the transducer preceding every Δp measurement. Once the two pressure taps were manually connected to the high and low pressure manifolds, the computer controlled procedure described below was initiated for the recording of the data.

Each measurement started with the pressure gauge shorted and the zero Δp output was first recorded. The pressure differential between the two taps was then measured across the 687 kPa (100 psi) range transducer. Once the pressure differential was calculated, the system automatically selected a pressure transducer such that the Δp to be measured would fall between 25 and 75 percent of the full range of the particular transducer chosen. With the chosen transducer, the computer measured the gauge's zero output when

shorted, then took 20 consecutive Δp readings, averaged them, and calculated their standard deviation. The same sequence was repeated once again and the new average of 20 new readings was compared to the last one calculated. If the two successive averages were within one percent of each other, the measurement was accepted and printed out as a data point. In addition, the instantaneous flow rate and other flow variables of interest were also recorded. If the two consecutive averages did not fulfill the acceptance criterion, the computer repeated this procedure until the criterion was met or until 15 sets of 20 readings each were made and the last output was printed as the data point. A typical output for an experiment is presented in Table III, which depicts the data acquisition format with the data, time, tap identity, pressure data, as well as various other instantaneous flow parameters of interest.

RESULTS AND DISCUSSION

In this section, results will be presented for the single phase nozzle calibration experiments, as well as pressure distributions and photographic observations under various flashing regimes.

A. Single Phase Calibration

The hydrodynamic calibration of the test section was done to determine the performance characteristics under single phase flow conditions and to obtain the axial distribution of the effective nozzle cross-sectional area.

Three main parameters were varied during these calibration tests: the mass flux (1.6-7.9 Mg/m^2sec), the inlet pressure (300-1000 kPa), and the

inlet temperature (23-149°C). These experiments covered a Reynolds number range from 9×10^4 to 9×10^5, based on test section inlet conditions. Typical pressure drop results with respect to the inlet, as a function of axial distance are presented in Fig. 2 for several flow conditions. In the converging section, the flow acceleration is accompanied by a pressure drop. The deceleration in the diverging section results in an expected pressure recovery. The pressure loss still apparent at the nozzle exit is representative of the friction losses. Figure 3 is a plot of the nondimensionalized pressure drop data obtained from 19 different experiments. The quantities ρ and U_o are the density and the velocity at the inlet of the test section. The dots represent the average of the pressure drop, and the bars the standard deviation of all the experiments performed. This deviation is < 5 percent in the converging section, reaches 6 percent at the throat, and is < 10 percent in the diverging section. The single curve corresponds to the pressure distribution expected, due tc acceleration only, and was calculated from the geometrical inside diameter measurements. This hydrodynamic calibration provides an effective hydrodynamic area distribution for the test section and will be used for comparison with the flashing data.

B. Pressure Distributions Under Flashing Conditions

Referring to a p-T diagram such as that in Fig. 4, showing the equilibrium vapor pressure p_{sat} of the liquid, the isothermal expansion of the test liquid in the nozzle may be represented by a vertical line A-B. Here, point A designates the nozzle inlet condition (p_{in}, T_{in}) and point B that at the throat. The distance A-B is directly related to the mass flux G through the

nozzle. Thus, for a given inlet condition, the saturation line may be crossed in the expansion if G is above a certain value.

Figure 5 presents typical pressure distributions obtained at inlet temperature of 100°C and four flow rates. At the low mass flux, 1.81 Mg/m^2s (Run 23), very little or almost no flashing was observed at all, and the results are very similar to the single phase calibration data. At the highest mass flux, 6.01 Mg/m^2s (Run 21), the pressure is observed to drop in the converging section up to the throat and level off from there onwards in the diverging section. A decrease in the mass flux, 4.90 Mg/m^2s (Run 20) and 5.90 Mg/m^2s (Run 28) is accompanied by a constant pressure region downstream of the throat followed by a pressure recovery region in the diverging section of the test section. This sudden pressure increase in the diverging section is caused by a condensation region to accommodate the back pressure imposed on the system. The dimensionless form of the pressure drop data presented in Fig. 5 are plotted in Fig. 6 vs the axial distance along the test section. The observations about the pressure recovery regions in the diverging section mentioned above are more obvious in this figure. The good agreement of the low mass flux no flashing pressure distribution results with the single phase calibration curve was interpreted to mean that no vapor was present in the pressure lines after the flashing experiments.

Similar experiments with flashing flows were also conducted at inlet temperatures of 124, 130, and 150°C for various flow rates. If one were to plot all these experiments on a p-T diagram like Fig. 4, it would be found that the saturation line was crossed at a location upstream and close to the

throat in each experiment. Thus we concluded that in all of the experiments reported in this paper, flashing occurred at a location close but upstream of the throat.

C. Operational Effects (Effect of Back Pressure)

In one set of experiments, flashing was initiated with the condensing tank liquid level (defined as the location of the free surface below the top of the tank) equal to zero, i.e., almost a solid loop condition. Decreasing the condensing tank liquid level, i.e., increasing the size of the steam cavity in the condensing tank, changed the downstream (condensing tank) pressure and affected the flashing conditions and pressure distriubutions although the flow rate and inlet conditions were held constant. Figure 7 depicts the pressure distribution results for these experiments, Runs 35, 37, and 43. The pressure distributions in the converging section and mass flux are observed to be independent of the downstream pressure, which imply that the flow is choked. Run 35 depicts the above-mentioned constant pressure region downstream of the throat followed by a sudden pressure rise, which seems to correspond to a condensation region as previously described. Runs 37 and 43 are almost identical although the condensing tank pressure is lower in Run 43.

The photographic observations performed during these experiments are presented in Fig. 8. For Run 35, the bubble sizes are minute, and their number density is very large. Decreasing the back pressure increases the vapor generated in Runs 37 and 43. During Run 43, the windows were covered with a water film, and the interior of the tube was invisible. This drastic

difference in observed appearance between Runs 37 and 43, does not noticeably affect the pressure distributions presented in Fig. 7.

D. Parametric Effects

The effects of the flow parameters, i.e., inlet pressure, p_{in}, inlet temperature, T_{in}, and mass flux, G, in the flashing regimes and pressure distributions were also investigated and will be presented below. Figure 9 presents the results when p_{in} and T_{in} were kept constant and the mass flux was varied close to conditions of flashing onset in the nozzle. This is equivalent to lengthening or shortening the line A-B in Fig. 4, moving the point B near the p_{sat} curve. The pressure distribution in the converging part follows very closely the single phase calibration. Downstream of the throat the vapor generation depicts itself as a deviation in the pressure distribution. This region is followed by a pressure increase caused by a sudden collapse of the bubbles and followed by a pressure recovery zone typical of single phase flows in divergent pipes. Figure 10 depicts the photographic observations for these two cases. Although the appearance of the bubbles was found to be intermittent, this fact was not apparent in the pressure measurements due to the time response of our pressure manifolds and to our long averaging times. In Fig. 11, we present the typical effect of a more substantial change in mass flux for an inlet temperature of 123°C and an inlet pressure of 260 kPa. At a mass flux of 2.01 Mg/m^2s (Run 57), one observes the onset of flashing, which intensified to violent flashing at a mass flux of 2.95 Mg/m^2s (Run 61). The photographic observations for Runs 57 and 61 are presented in Fig. 12.

The effect of changing the inlet temperature from 100 to 150 °C was also investigated while maintaining a fixed initial overpressure, $p_{in} - p_{sat}(T_{in})$. This corresponds to moving the point A parallel to the saturation curve p_{sat}, in Fig. 4 and keeping the mass flux unchanged. For constant values of the pressure difference between the inlet pressure and the saturation pressure at the inlet temperature, i.e., $p_{in} - p_{sat}\ (T_{in})$, the effect of inlet temperature on the pressure distributions was not very pronounced for the various flashing experiments. This behavior was to be expected, since the driving potential, i.e., $(p - p_{sat})$ was not changed in these runs.

Finally, the influence of variation of p_{in}, i.e., moving the point A in Fig. 4 up and down without changing anything else, was studied. A slight variation of the inlet pressure was found to affect the pressure distributions and flashing regimes for identical inlet temperatures and mass fluxes. This dependence and sensitivity is more pronounced at low mass fluxes, Fig. 13 (Runs 55 and 58 with an inlet temperature of $\sim$ 123.4°C and mass flux of 2.98 Mg/m^2s). A variation of the inlet pressures from 296 kPa (Run 55) to 257 kPa (Run 58) shows a marked variation in the pressure distributions in the diverging section of the nozzle. This marked dependence observed for the low mass fluxes does not repeat itself at the higher mass fluxes, 4.96 Mg/m^2sec, as presented in Fig. 14, for an inlet temperature of 100 °C (Runs 45, 37, and 43).

CONCLUSIONS AND FUTURE DIRECTIONS

In order to measure the steady state vapor generation rates under

nonequilibrium conditions, a flow loop with well controlled flow and thermodynamic conditions was designed, built and made operational. The test section consisting of a converging-diverging nozzle was first calibrated hydrodynamically with single phase flows. Pressure distributions were recorded along the test section and photographic observations made at the exit of the test section under various flashing regimes. With flashing occurring close to, but upstream of the throat, the pressure distribution in the converging section was observed to follow closely the single phase calibration results. In the diverging section of the nozzle, either a continuous constant pressure distribution was observed all along this region or the constant pressure was followed by a sudden pressure increase (condensation shock) and a single phase-like pressure recovery.

Variation of the back pressure revealed a choked flow pattern in the converging section of the nozzle. Depending on the back pressure, the pressure distributions in the diverging sections showed the presence of a condensation shock. In the absence of condensation shocks in the test section, marked variations were seen in the photographic observations at different back pressures, but corresponding variations were not observed in pressure distributions.

During the investigation of the parametric effects, the mass flux and inlet pressures were found to have a stronger effect on the pressure distributions and photographic observations than variations in the inlet temperatures under constant $p_{in} - p_{sat}\ (T_{in})$ conditions. These parametric effects were more visible at low mass fluxes at the onset of flashing than at higher ones. The flashing onset was also observed to be an intermittent phenomenon.

The net vapor generation calculations from the experimental data needs, in addition to the pressure profiles, the axial and radial void fraction measurements by means of γ-densitometry which are being conducted presently.

ACKNOWLEDGEMENT

This research was sponsored by the U. S. Nuclear Regulatory Commission.

The authors wish to thank Ms. Nancy Schneider for her efforts in the preparation and typing of the manuscript.

REFERENCES

1. Hsu, Y. Y., "Review of Critical Flow, Propagation of Pressure Pulse and Sonic Velocity," NASA TND-6814, 1972.

2. Saha, P., "Review of Two-Phase Steam-Water Critical Flow Models With Emphasis on Thermal Nonequilibrium," NUREG/CR-0417, BNL-NUREG-50907, 1978.

3. Seynhaeve, J. M., "Critical Flow Through Orifices," Paper presented at the European Two-Phase Flow Group Meeting, Grenoble, 1977.

4. Isbin, H. S., Moy, J. E., and DaCruz, A.J.R., "Two-Phase Steam-Water Critical Flow, AIChE J3, 361, 1957.

5. James, R., "Steam-Water Critical Flow Through Pipes," Proc. Instn. Mech. Engrs., 176, 2, 741-748, 1962.

6. Ardron, K. H. and Ackerman, M. C., "Studies of the Critical Flow of Subcooled Water in a Pipe," Paper presented at the CSNI Specialist Meeting on Transient Two-Phase Flow, Paris, 1978.

7. Reocreux, M. and Seynhaeve, J. M., "Ecoulements diphasiques eau-vapeur: essais comparatifs de debits critiques," Acta Technica Belgica EPE Vol X, 3-4, 115-137, 1974.

8. Fauske, H. K., "The Discharge of Saturated Water Through Tubes," Chem. Eng. Prog. Sym. Ser., 61, 210-216, 1965.

9. Reocreux, M., Contribution a l'etude des debits critiques en ecoulements diphasiques eau-vapeur, These de Dodorat, Universite Scientifique et Medicale de Grenoble, 1974.

10. Silver, R. S., "Temperature and Pressure Phenomena in the Flow of Saturated Liquids, Proceedings of the Royal Society of London, Series A, Vol. 194, 17, 1948.

11. Zaloudek, F. R., "The Critical Flow of Hot Water Through Short Tubes," HW-77594, 1963.

12. Fauske, H. K. and Henry, R. E., "The Two-Phase Critical Flow of One-Component Mixtures in Nozzles Orifices and Short Tubes, J. of Heat Transfer, 464, 1971.

13. Schrock, V. E., Starkman, E. S., and Brown, R. A., "Flashing Flow of Initially Subcooled Water in Convergent Divergent Nozzles," presented at the ASME-AIChE Heat Transfer Conference, St. Louis, MO, 1976.

REFERENCES (Cont'd)

14. Simoneau, R. J., "Pressure Distribution in a Converging-Diverging Nozzle During Two-Phase Choked Flow of Subcooled Nitrogen, NASA TMX-71762, 1975.

15. Hendricks, R. C., Simoneau, R. J., and Burrows, R. F., "Two-Phase Choked Flow of Subcooled Oxygen and Nitrogen," NASA TN D-8169, 1976.

TABLE I

OPERATING CONDITIONS

Test Section Inlet Pressure	100 - 1000 kPa
Test Section Inlet Temperature	20 - 150°C
Mass Flux	1.0 - 7.8 Mg/m^2sec
Reynolds Number Based on Inlet Conditons	10^5 - 10^6

Converging Test Section Inlet Conditions From Subcooled To Low Qualities

TABLE II

TEST SECTION INSTRUMENTATION

QUALITY MEASURED	TYPE OF SENSOR	RANGE	ACCURACY
Temperature	Resistance Temp. Detector (RTD)	-200 to 500°C	1.2% @ 200°C
Differential Pressure	Strain Gage Δp Transducer	4 to 500 kPa	1% of Reading
Flow Rate	Turbine Meter	3 to 950 ℓ/min	0.5% Full Scale
Void Fraction	Gamma Densitometer (Thulium/Cad-Telluride)	0 to 1	5% Steady State (Future 5% per 1 ms)

BNL FLASHING FLOWS EXPERIMENT
PRESSURE DROP DATA FROM
TEST SECTION # 2

RUN NUMBER 70

DP. MEAS. CZLIBRATION

1656 26JAN79

TAPS	LOOP FLOW GPM	LOOP FLOW LTR/SEC	TEMPERATURES (DEG F) FLOW METER	TS INLET	COND TANK	PRESSURE (PSIA) TS INLET	COND TANK	VELOCITY CM SEC	REYNOLDS NUMBER	DIFFERENTIAL PRESSURE MEASURED	DIMENSIONLESS
1-2	108.5	6.8	117.4	128.7	119.1	30.8	29.2	336.9	.326E+06	.01	.01
1-4	109.1	6.9	117.4	128.7	118.8	30.7	29.0	339.0	.328E+06	.09	.11
1-6	108.5	6.8	117.4	128.8	118.9	30.6	28.8	337.2	.327E+06	.31	.37
1-7	108.9	6.9	117.5	128.8	118.5	30.7	29.1	338.2	.328E+06	.39	.47
1-9	109.4	6.9	117.5	128.8	118.8	30.7	29.0	339.9	.329E+06	.71	.85
1-11	108.3	6.8	117.6	128.9	118.4	30.6	29.0	336.6	.326E+06	1.14	1.40
1-13	108.8	6.9	117.6	128.9	118.6	30.6	29.2	338.1	.328E+06	1.68	2.04
1-14	109.1	6.9	117.6	128.9	119.3	30.6	29.0	339.0	.329E+06	2.03	2.45
1-15	108.5	6.8	117.6	128.9	119.9	30.6	29.1	337.0	.327E+06	2.36	2.88
1-16	108.9	6.9	117.6	128.9	118.9	30.6	29.2	338.2	.328E+06	2.78	3.37
1-17	109.1	6.9	117.6	128.8	119.5	30.6	29.3	339.0	.329E+06	3.50	4.22
1-18	109.4	6.9	117.6	129.0	118.5	30.8	29.0	339.8	.330E+06	4.05	4.87
1-19	108.4	6.8	117.6	129.0	119.9	30.7	29.1	336.7	.327E+06	4.56	5.58
1-20	108.8	6.9	117.6	129.0	118.9	30.7	29.0	338.1	.328E+06	5.50	6.67
1-21	109.1	6.9	117.6	129.0	119.4	30.8	29.2	339.0	.329E+06	6.51	7.86
1-22	108.0	6.8	117.7	129.1	119.5	30.7	29.1	335.4	.326E+06	8.26	10.19
1-23	109.3	6.9	117.7	129.2	119.3	30.6	29.1	339.6	.330E+06	9.63	11.59
1-24	107.8	6.8	117.8	129.3	119.1	30.7	29.2	334.8	.326E+06	11.65	14.42
1-25	108.8	6.9	117.8	129.3	119.5	30.8	29.1	338.0	.329E+06	15.05	18.29
1-26	108.6	6.9	117.9	129.4	119.0	30.6	29.1	337.5	.329E+06	12.06	14.70
1-27	108.9	6.9	118.0	129.4	119.3	30.6	29.0	338.4	.330E+06	10.08	12.22
1-28	108.6	6.9	118.0	129.5	119.9	30.7	29.1	337.4	.329E+06	8.80	10.73
1-29	108.9	6.9	118.0	129.5	119.2	30.8	29.0	338.4	.330E+06	7.37	8.94
1-30	107.9	6.8	118.0	129.5	119.6	30.9	29.1	335.1	.327E+06	6.59	8.15
1-31	108.5	6.8	118.1	129.6	119.5	30.6	29.1	337.2	.329E+06	5.73	7.00
1-32	109.0	6.9	118.1	129.5	118.6	30.7	28.9	338.8	.330E+06	5.22	6.31
1-33	108.3	6.8	118.1	129.6	119.9	30.6	28.9	336.4	.328E+06	4.67	5.72
1-34	109.2	6.9	118.1	129.6	119.6	30.8	29.1	339.1	.331E+06	4.22	5.10
1-35	108.4	6.8	118.1	129.6	119.8	30.7	29.1	336.6	.328E+06	3.85	4.71
1-36	108.7	6.9	118.1	129.6	119.9	30.9	29.2	337.6	.329E+06	3.59	4.38
1-37	109.1	6.9	118.1	129.6	119.8	30.8	29.1	338.9	.330E+06	3.34	4.03
1-38	108.6	6.9	118.1	129.5	119.7	30.8	29.1	337.4	.329E+06	3.10	3.78
1-39	108.9	6.9	118.1	129.5	120.3	30.8	29.2	338.2	.330E+06	2.88	3.50
1-40	108.5	6.8	118.1	129.6	120.3	30.8	29.2	336.9	.329E+06	2.69	3.28
1-41	108.5	6.8	118.1	129.6	119.6	30.7	29.0	337.2	.329E+06	2.50	3.05
1-42	108.7	6.9	118.1	129.6	120.0	30.6	29.0	337.8	.330E+06	2.39	2.91
1-43	107.9	6.8	118.1	129.6	119.7	30.8	29.0	335.4	.327E+06	2.23	2.75
1-44	108.6	6.8	118.1	129.6	120.0	30.6	29.1	337.2	.329E+06	2.14	2.61
1-45	109.0	6.9	118.2	129.6	119.1	30.5	28.8	338.6	.330E+06	2.03	2.45
1-46	108.8	6.9	118.1	129.7	119.7	30.7	29.2	338.1	.330E+06	1.93	2.35
1-47	108.6	6.9	118.2	129.6	119.6	30.6	29.0	337.5	.329E+06	1.87	2.28
1-48	108.5	6.8	118.1	129.6	119.5	30.6	28.9	337.0	.329E+06	1.83	2.24
1-49	108.8	6.9	118.2	129.6	119.4	30.7	29.0	337.9	.330E+06	1.77	2.15

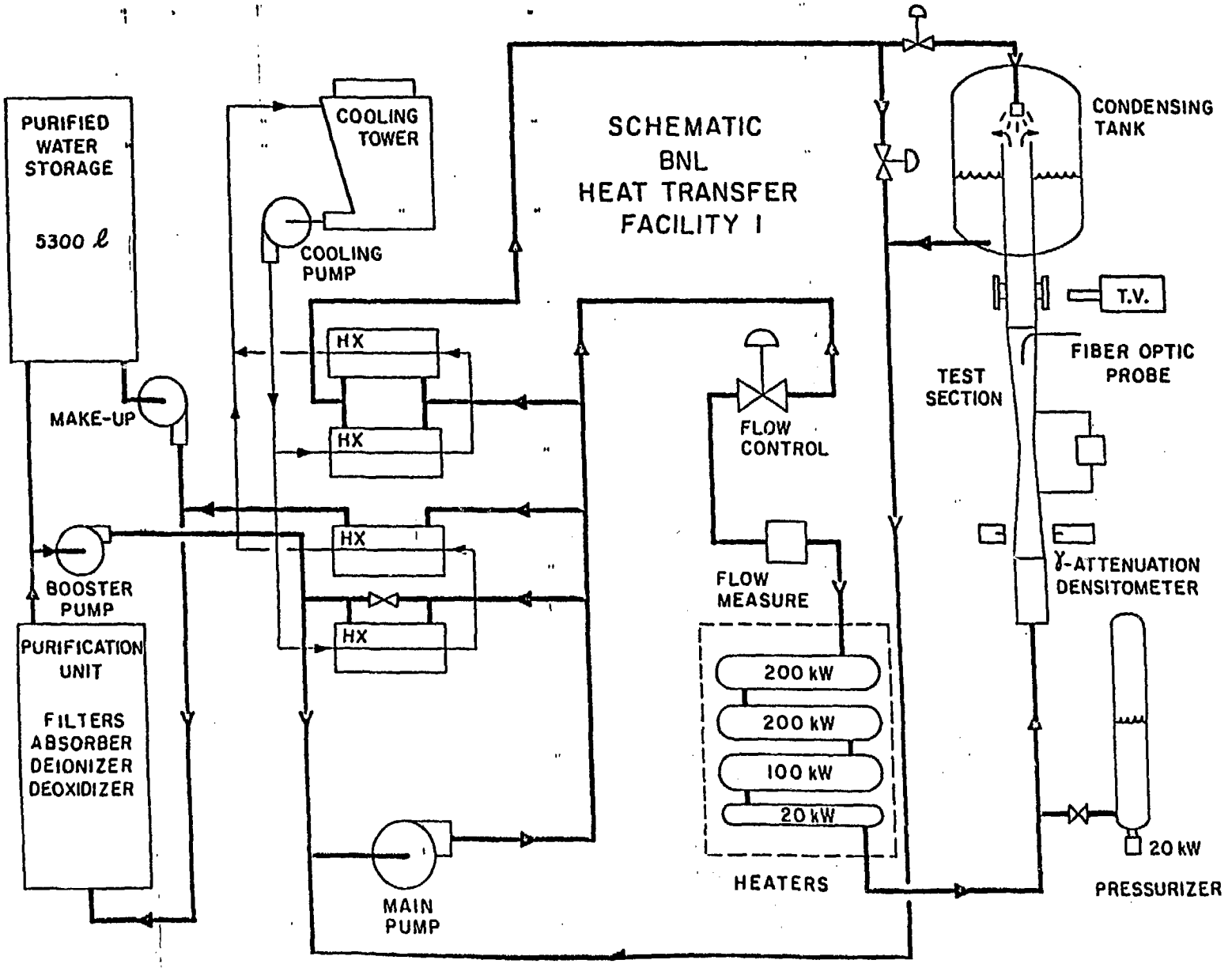

1-1246-79

Figure 1 - Schematic of BNL Heat Transfer Facility 1 (BNL Neg. No 1-1246-79)

SYMBOL	EXP	Q(LPM)	Re_D	P_{50}(kPa)	T_{in}(C)
o	10	191.1	93400	725.1	27
□	9	383.3	187650	727.8	27.1
◇	8	576.5	281000	722.3	26.9
△	7	770.6	378900	729.2	27.3
×	6	857.8	425500	727.8	27.7

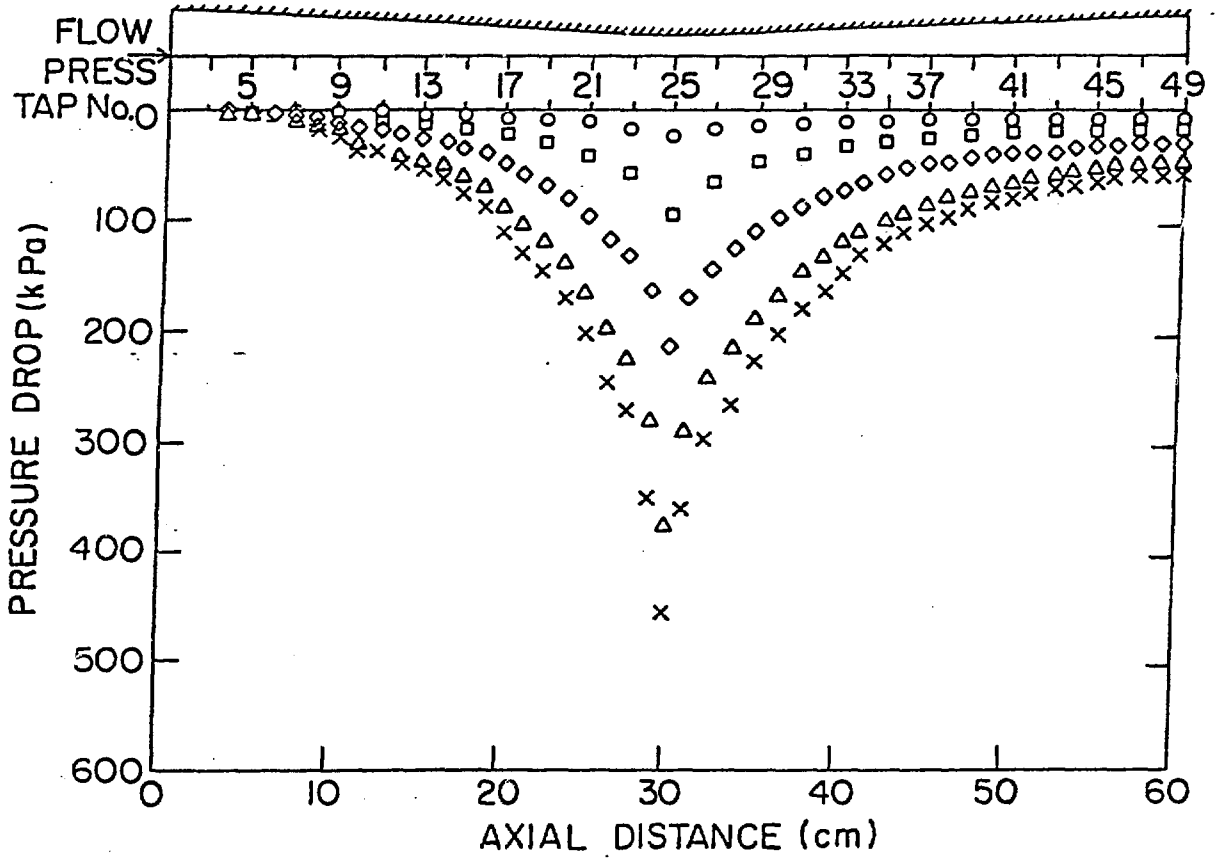

Figure 2 - Typical Pressure Distributions Along TS-2 for the Single-Phase Flow Hydrodynamic Calibration Runs. (BNL-NEG NO. 10-506-78)

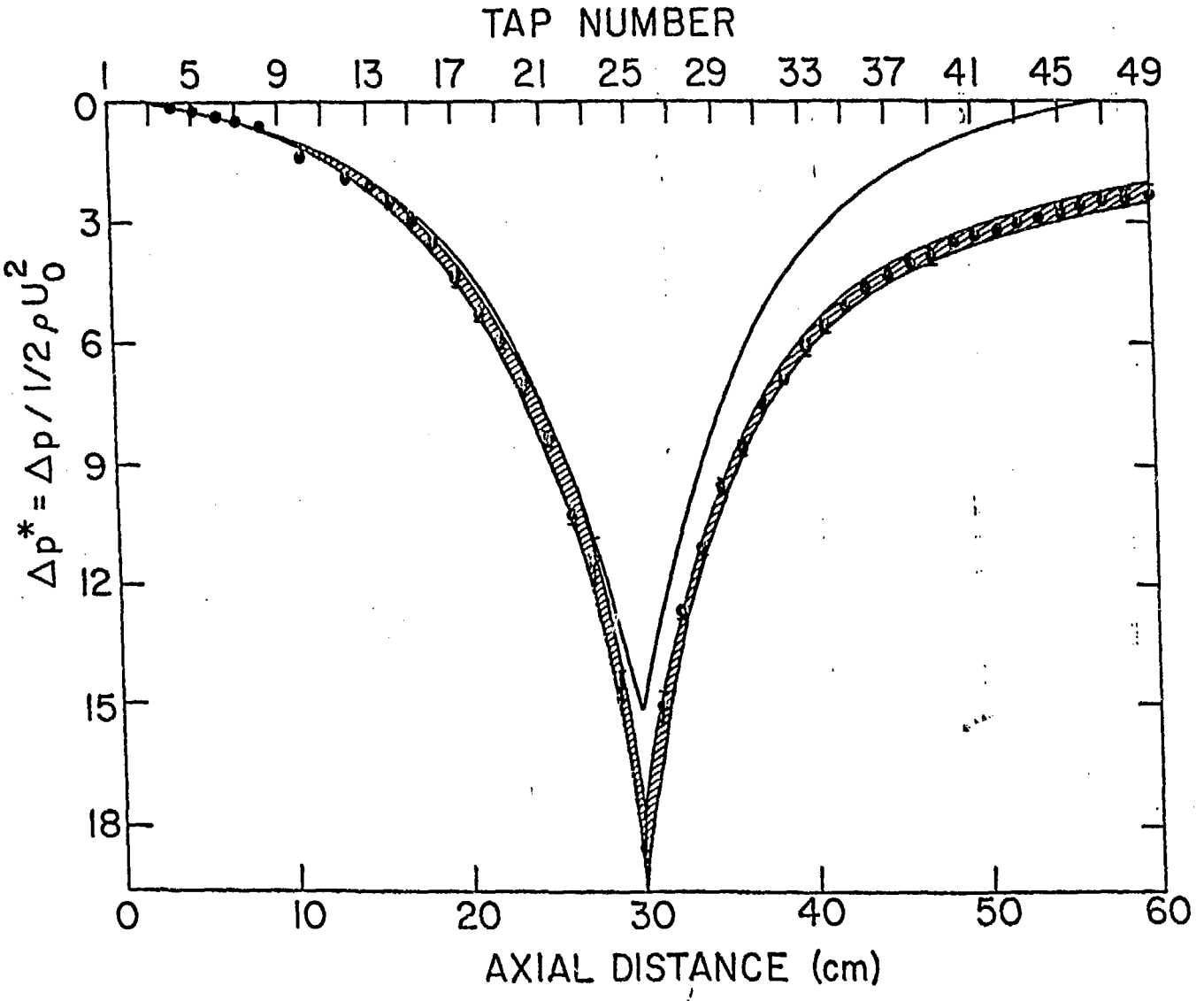

Figure 3 - Dimensionless Pressure Distribution for TS-2. Data is Averaged for all the Hydrodynamic Calibration Runs Performed. (BNL NEG. NO. 10-503-78)

10-503-78

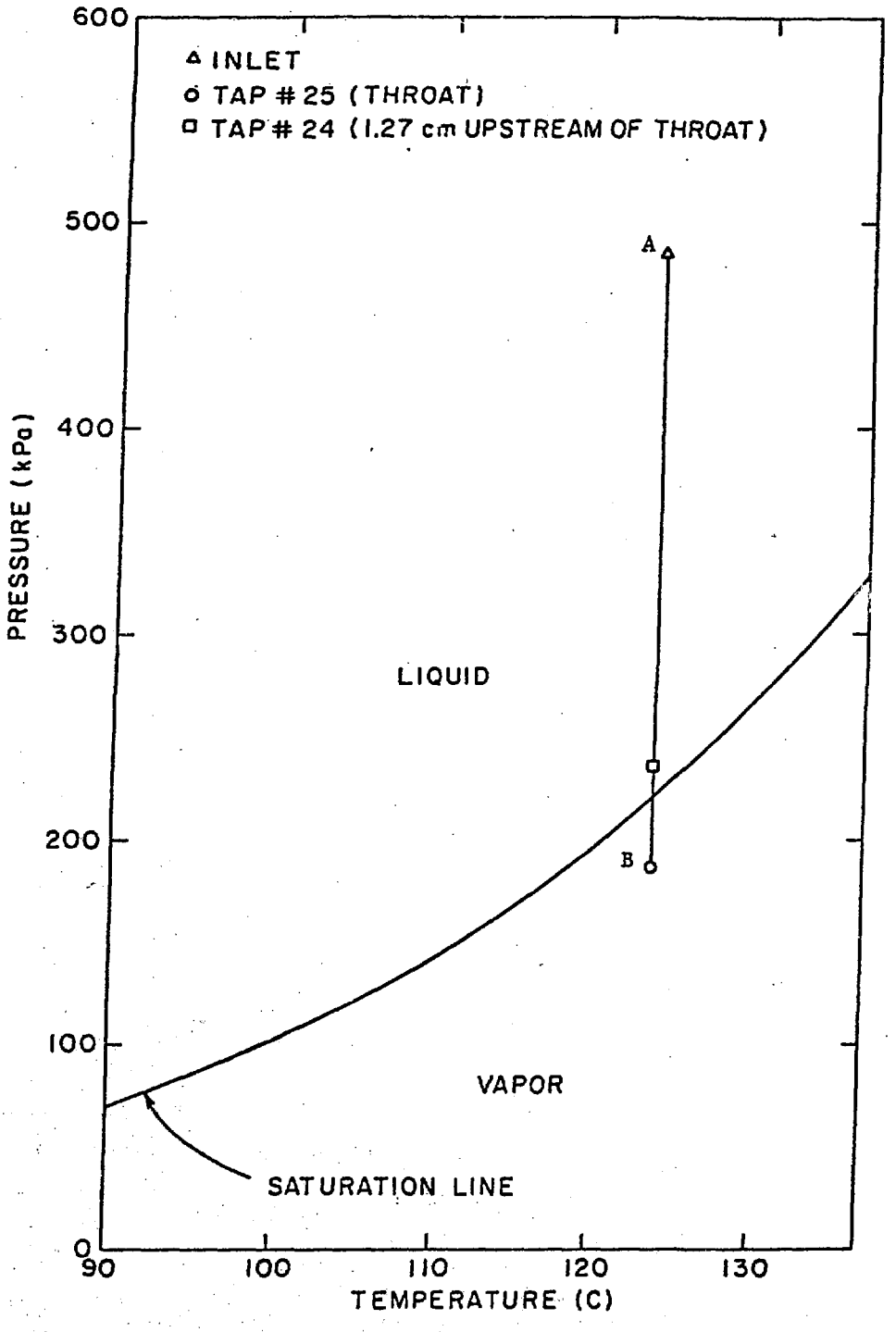

Figure 4 - Typical representation of an isothermal flashing experiment in the p-T diagram. (No BNL Neg. No).

SYMBOL	EXP	P_{50} (kPa)	T_{in}(C)	Q(LPM)	Re
◇	23	146.4	99.4	229.2	323 300
□	28	190.4	100.2	386.6	549 800
△	20	313	99.6	621.6	878 800
○	21	433.5	100.6	763.1	1089 000

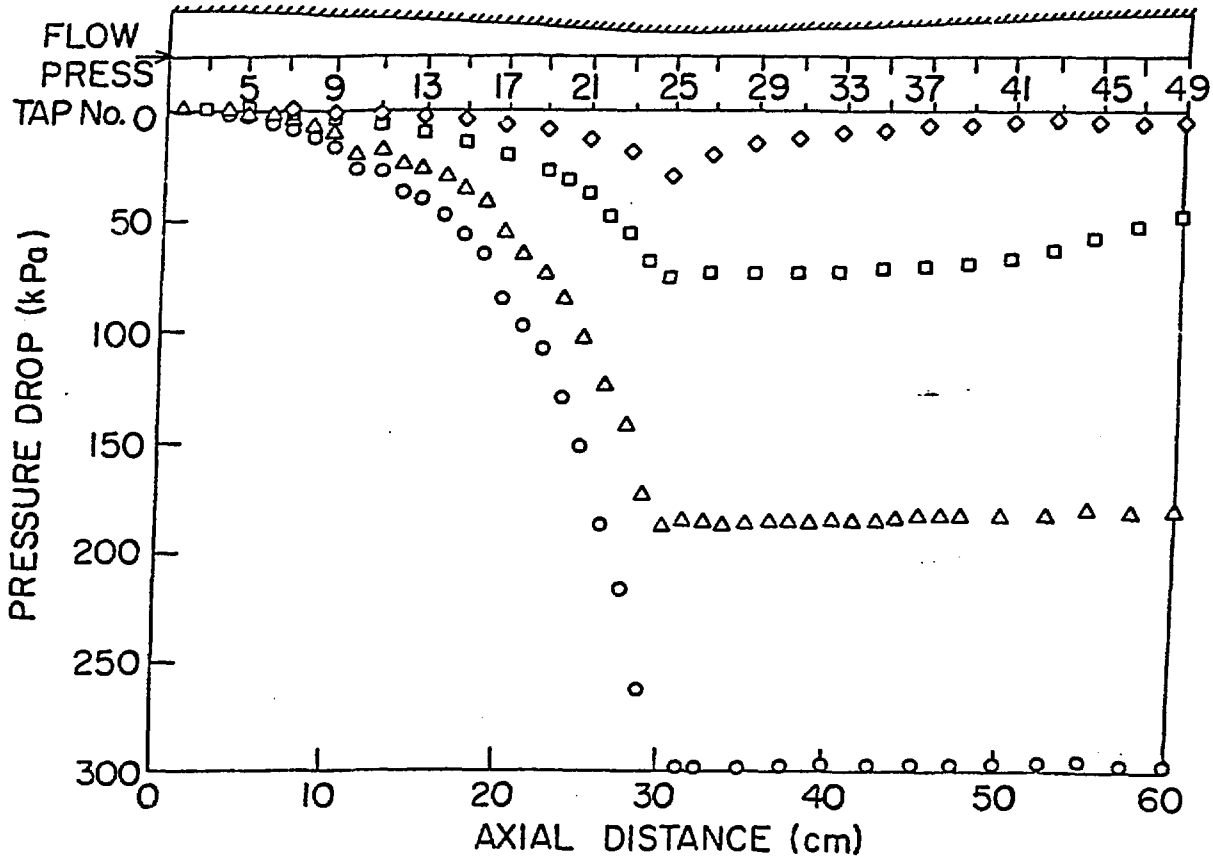

Figure 5 - Pressure Distributions Under Flashing and Non-Flashing Conditions in TS-2. (BNL-NEG. NO. 10-505-78)

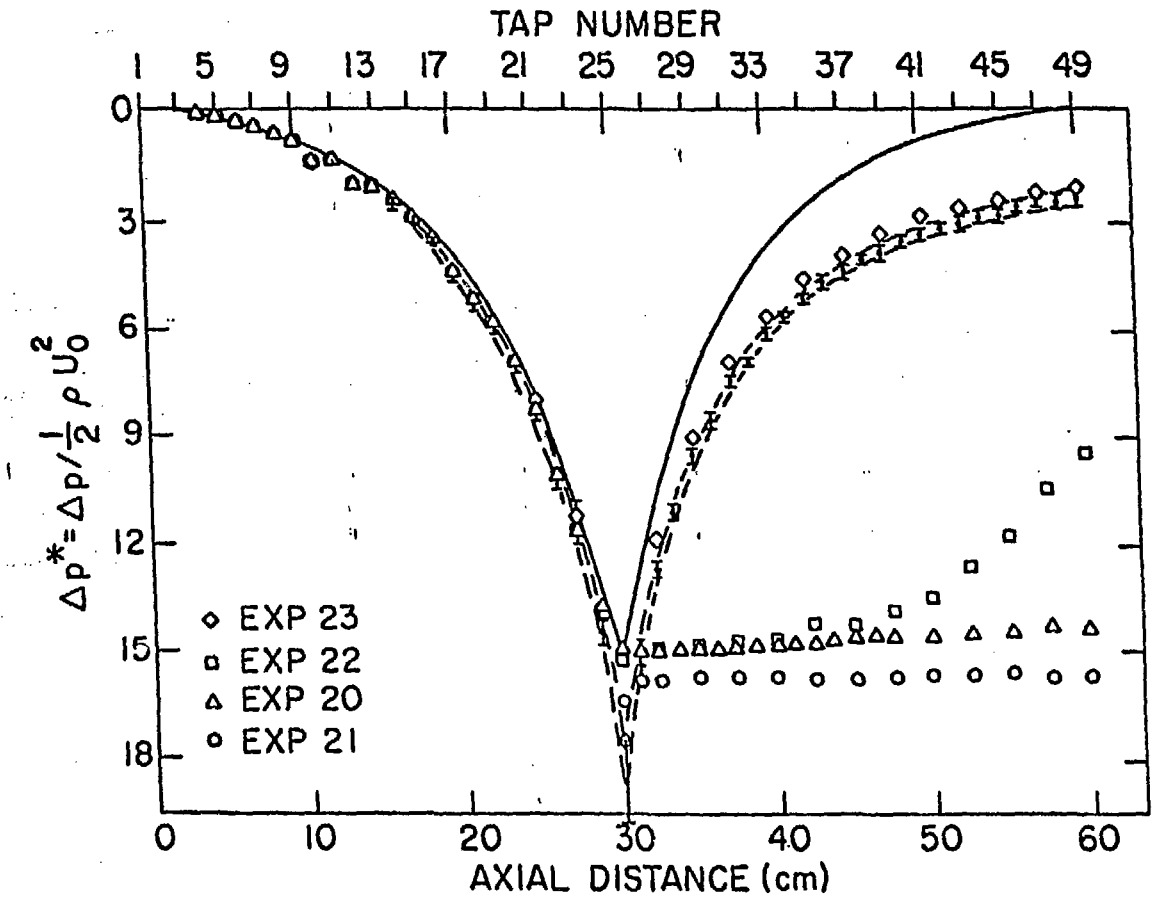

Figure 6 - Dimensionless Pressure Distribution in TS-2 Under Flashing Conditions as Compared to Single-Phase Hydrodynamic Calibration Data. (BNL-NEG. NO. 10-500-78).

10-500-78

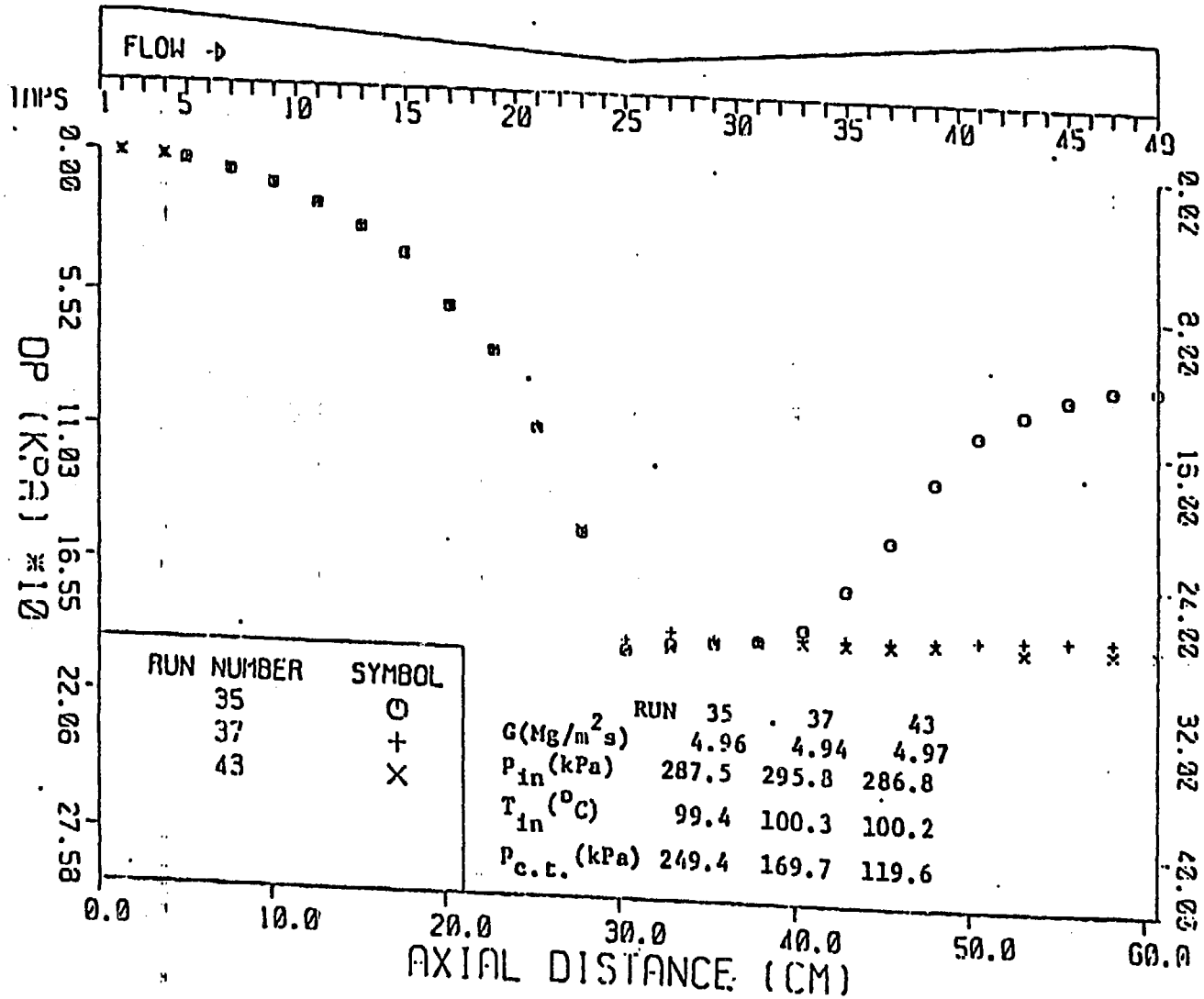

Figure 7 - Pressure distributions showing the effect of condensing tank back pressure for identical nozzle inlet conditions (BNL Neg. No 1-728-79).

1-728-79

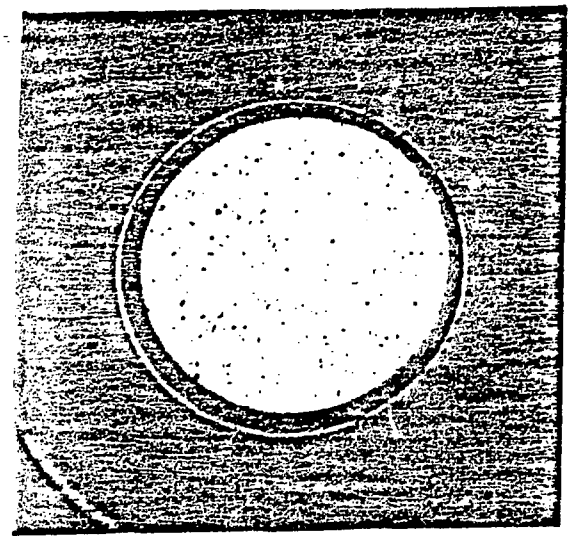

A. RUN NO. 35

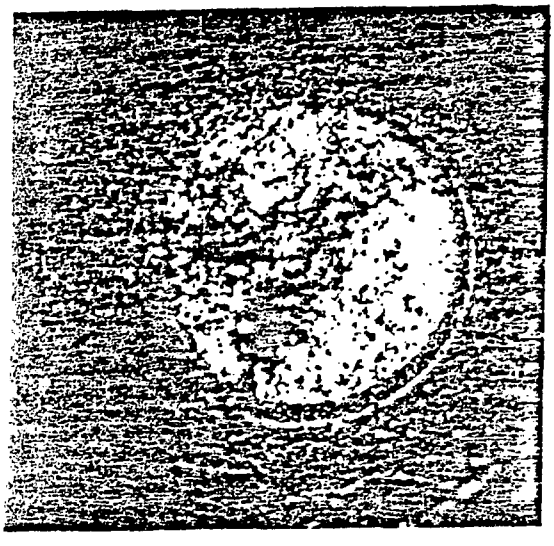

B. RUN NO. 37

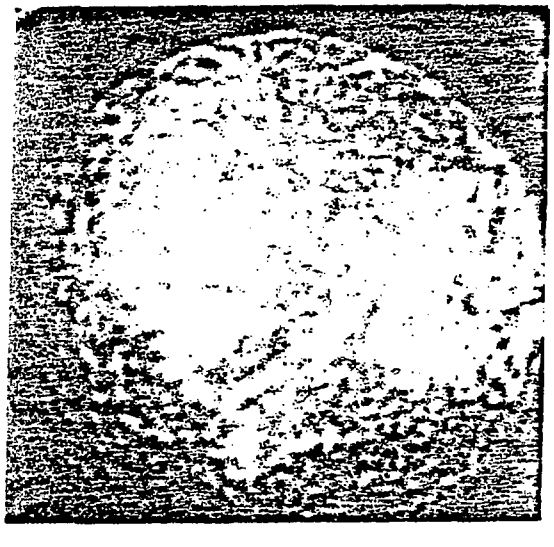

C. RUN NO. 43

SCALE 1:1

Figure 8 - Photographic observations for the experimental conditions presented in Fig. 7 (BNL Neg. No 1-919-79).

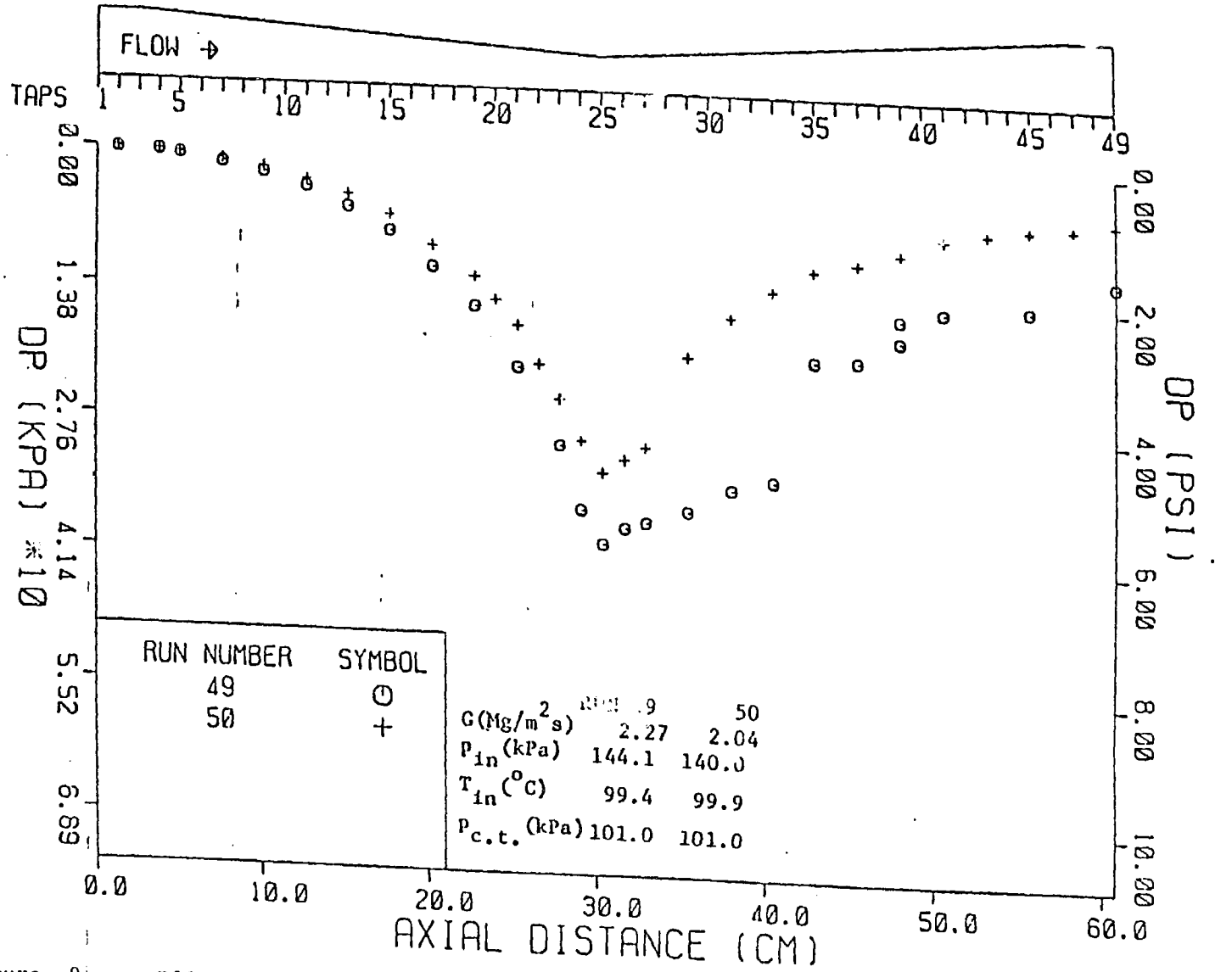

Figure 9 - Effect of mass flux on pressure distributions for identical nozzle inlet conditions which are close to the onset of flashing in the test section (BNL Neg. No 1-727-79).

1-727-79

SCALE 1:1

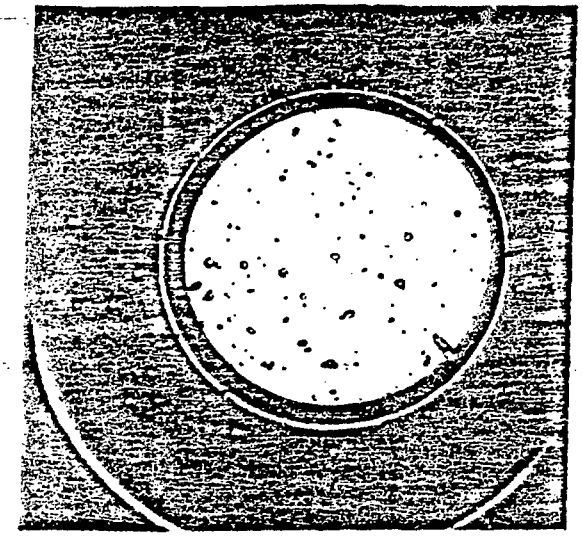

RUN NO. 49

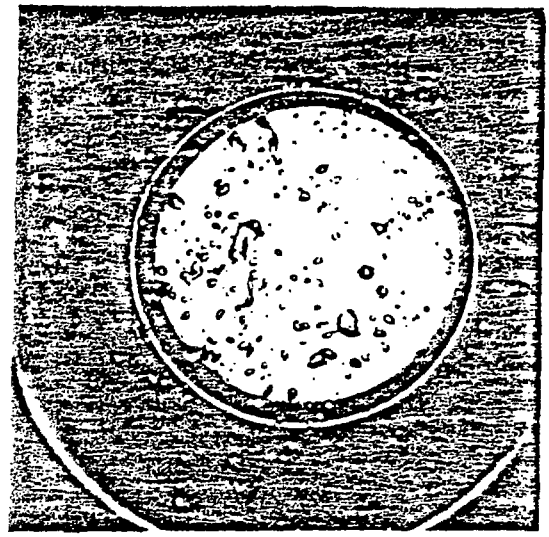

RUN NO. 49

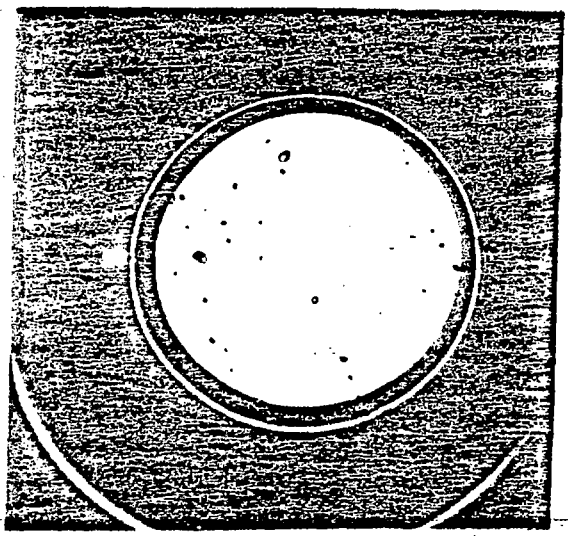

RUN NO. 50

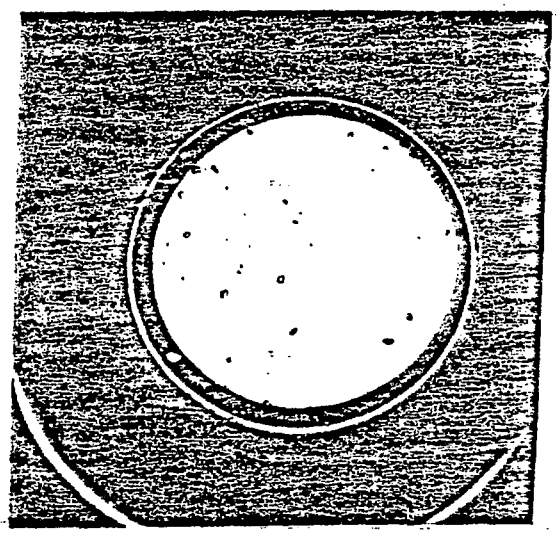

RUN NO. 50

Figure 10 - Photographic observations for the experimental conditions presented in Fig. 9 (BNL Neg. No 1-922-79).

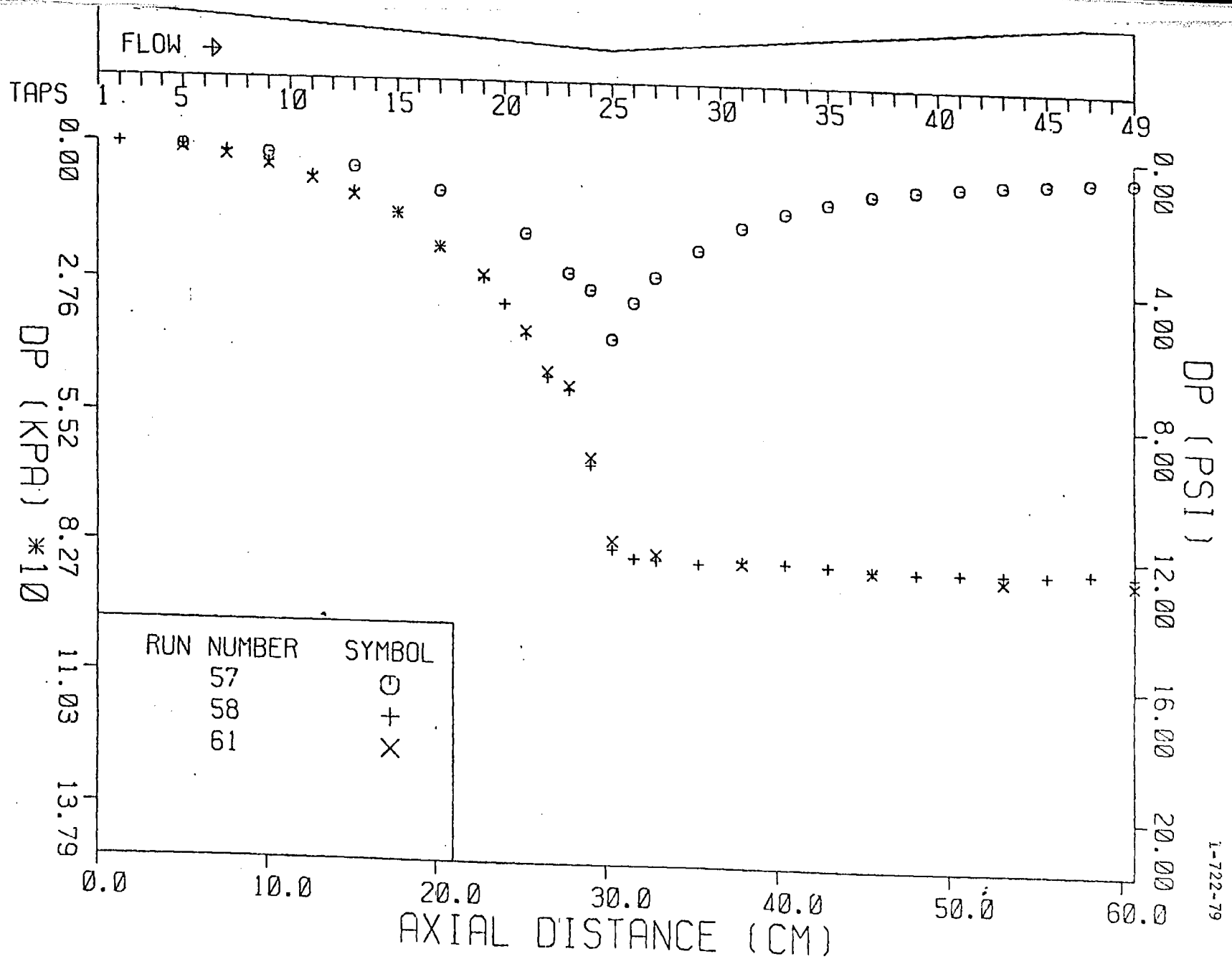

Figure 11 - Effect of mass flux on the pressure distribution in the test section (BNL Neg. No 1-722-79).

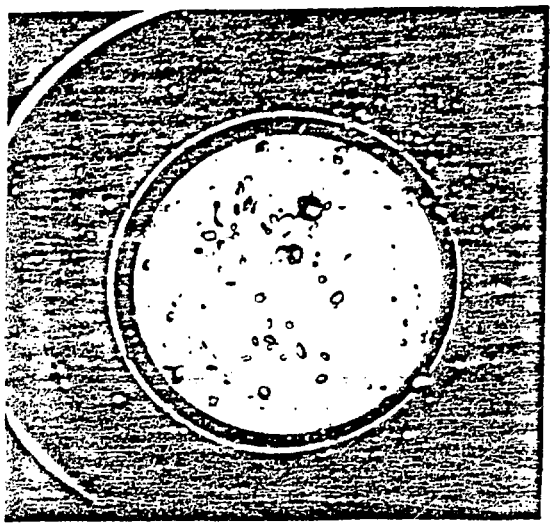

RUN NO. 57

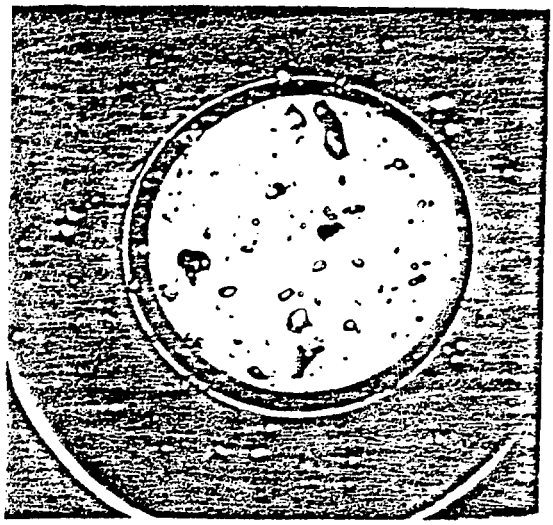

RUN NO. 57

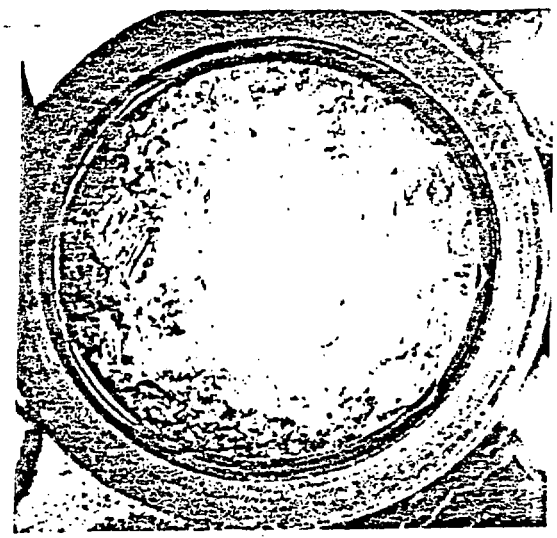

RUN NO. 61

SCALE 1:1

Figure 12 - Photographic observations for the experimental conditions presented in Fig. 11 (BNL Neg. No 1-918-79).

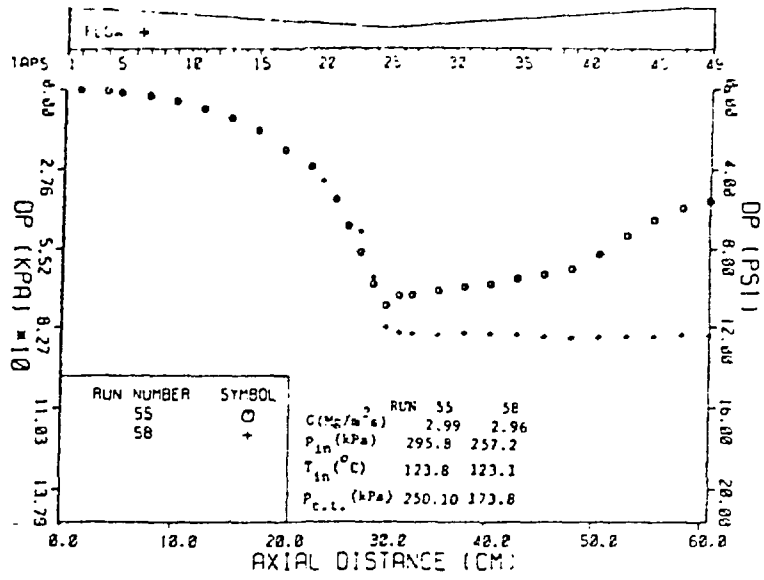

Figure 13 - Effect of nozzle inlet pressure on the pressure distributions in the test section (BNL Neg. No 1-719-79).

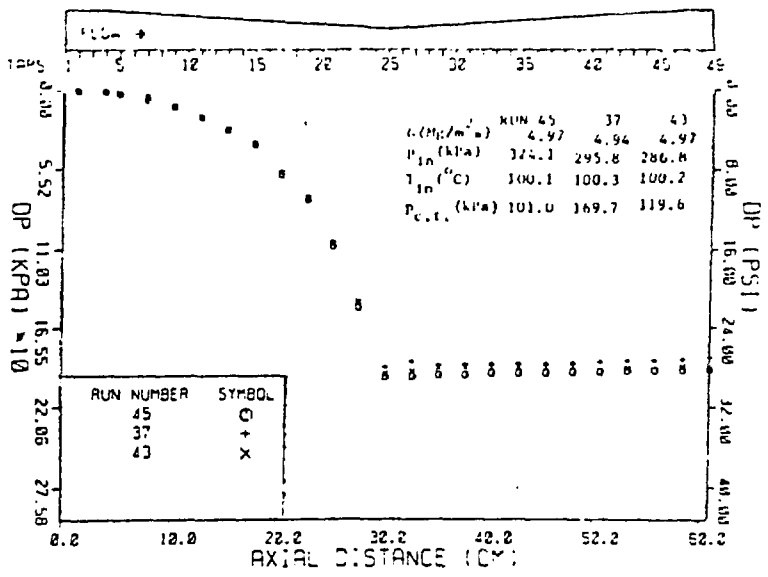

Figure 14 - Effect of nozzle inlet pressure on the pressure distributions in the test section (BNL Neg. No 1-717-79).